Available online at www.sciencedirect.com
ScienceDirect
Trans. Nonferrous Met. Soc. China 33(2023) 2272−2286
Transactions of Nonferrous Metals Society of China
www.tnmsc.cn

Ductile fracture behavior of in situ TiB_2 particle reinforced 7075 aluminum matrix composite in various stress states

Han WANG, Hai-ming ZHANG, Zhen-shan CUI, Zhe CHEN, Dong CHEN

School of Materials Science and Engineering, Shanghai Jiao Tong University, Shanghai 200240, China

Received 13 February 2022; accepted 2 June 2022

Abstract: The fracture behavior of an in situ TiB_2 particle reinforced 7075 aluminum matrix composite in various stress states was investigated by mechanical tests, microscopic characterization, and numerical simulations. Four sets of tensile specimens, one group of shear specimens, and one group of compression specimens were designed, and mechanical experiments were conducted on these six groups of specimens. The strain distributions of the six groups of specimens during deformation were investigated by in situ strain testing and finite element simulation. The fracture morphology of the specimens was characterized to analyze the damage mechanism in different stress states. It was found that the fracture mechanism of the material is mainly interfacial debonding and particle fracture, manifested as tensile fracture under high stress triaxiality and shear fracture under low stress triaxiality. For the tensile fracture, the nucleated voids grew with the maximum principal stress; for the shear fracture, they showed significant shape change with the maximum shear stress but little volume change. Based on the fracture mechanisms uncovered by the experiments, a modified ductile fracture criterion, considering the influence of both the maximum principal stress and maximum shear stress, was developed for the composite. Comparison with the modified Mohr−Coulomb, Lou−Yoon−Huh, Hu, and Mu models shows that the proposed model can predict the ductile fracture behavior of the aluminum matrix composites more accurately.

Key words: aluminum matrix composite; ductile fracture criterion; interface debonding; particle fracture

1 Introduction

The particle reinforced aluminum matrix composites (PR-AlMCs) have wide application prospects as structural materials because of their excellent mechanical properties of high strength, high stiffness, and good toughness [1,2]. In particular, in situ PR-AlMCs have received increasing attention as the in situ particles show better cohesion with the matrix, which effectively improves the strength and modulus of the composite [3,4]. In practice, PR-AlMC components are subjected to complex stress states during the forming process or loading service thus, it requires a full understanding on their fracture mechanism in different stress states.

Due to the significant difference of mechanical properties between particles and matrix, PR-AlMCs exhibit a complex fracture behavior and generally have three fracture mechanisms, i.e., particle fracture, interface debonding between reinforced particles and matrix, and void nucleation and growth in the matrix [5]. LLOYD [6] studied the tensile failure behavior of a SiC/6061Al composite, and found that the main failure mechanism of the composite with coarse particles (above 20 μm) is particle fracture, and that with fine particles (below 5 μm) is void nucleation and growth in matrix. Similar phenomena were reported in the SiC/7075Al composite [7] and Si/Al composite [8]. KARBALAEI AKBARI et al [9] investigated the

Corresponding author: Hai-ming ZHANG, Tel: +86-21-62813430-8019, E-mail: hm.zhang@sjtu.edu.cn;
Zhen-shan CUI, Tel: +86-21-62827605, E-mail: cuizs@sjtu.edu.cn
DOI: 10.1016/S1003-6326(23)66258-2

tensile fracture mechanisms of a nano TiB_2/A356Al composite with different particle contents, and found that void evolution and interface debonding are two main fracture mechanisms of the composite. WU and ARSENAULT [10] investigated the crack propagation in a SiC_p/Al composite by in situ SEM observation; the results show that cracks mainly expand along the fractured particles. The interface bonding strength also determines the fracture mechanism of composites; cracks initiate more easily at weak interfaces via interface debonding. These previous studies shed important insight into the failure mechanisms of composites. Nevertheless, it should be noted that these studies mainly focused on the fracture behavior of composites under uniaxial loading. An in-depth understanding on the influence of stress states on the fracture mechanism of PR-AlMCs is still lacking.

Regarding the quantitative description of the fracture behavior, ductile fracture criteria (DFCs) are efficient tools and commonly used. DFCs can be classified into two categories, i.e., the coupled and uncoupled DFCs. The coupled DFCs incorporate the interaction of plastic deformation and damage accumulation. The representative coupled DFCs are the micromechanics-based Gurson−Tvergaard−Needleman (GTN) model [11] and the continuum damage mechanics model [12]. The uncoupled DFCs are primarily empirical models based on experiments, micromechanical analysis, and numerical simulation. These models do not consider the influence of damage on the constitutive responses of materials. Due to the simple form and fewer parameters to be determined, the uncoupled DFCs have recently received much attention [13−15]. For example, BAO and WIERZBICKI [16] investigated the fracture behavior of Al 2024-T351 in a wide range of stress triaxiality (from 0.3 to 1.0), and developed the Bao-Wierzbicki DFC to establish the fracture surface of the material. The early DFCs were generally designed for deformation conditions with high stress triaxiality (from 1/3 to 2/3), and the applicability of the models in the circumstances of low or negative stress triaxiality (from −1/3 to 1/3) is not clear [17]. XUE [18] and XUE and WIERZBICKI [19] found that the fracture strain of Al 2024-T351 in shear deformation is smaller than that in uniaxial tensile deformation. Shear stress is represented by the Lode parameter, and two phenomenological DFCs considering both stress triaxiality and the Lode parameter were established by XUE [18] and XUE and WIERZBICKI [19]. BAI and WIERZBICKI [20] proposed a modified Mohr−Coulomb criterion (MMC) to describe the ductile fracture of metals, and the MMC criterion fitted well with the experimental data of Al 2024-T351. Based on the micro-mechanism of fracture, LOU et al [21] proposed a DFC which considers the ductile fracture of metals induced by void nucleation, growth, and coalescence. Subsequently, LOU et al [22] extended the above DFC by introducing a cutoff value for predicting the fracture strain in the case of stress triaxiality below −1/3. The above studies mainly focus on the ductile fracture of traditional metals, while paying less attention to materials with reinforced particles.

Although many investigations have been conducted on the fracture mechanisms of composites, a comprehensive understanding on the fracture mechanism for the in-situ PR-AlMCs at different stress states is still insufficient. Besides, an efficient DFC for in situ PR-AlMCs is of urgent need. In this work, the fracture mechanisms of an in situ 6 wt.% TiB_2 particle reinforced aluminum matrix composite were investigated through experiments and fractograph characterization in various stress states. An uncoupled DFC was developed based on the fracture mechanisms obtained above. DIC experiments and numerical simulations were carried out to estimate the state variables of fracture. To validate the accuracy and feasibility of the proposed DFC, the results were compared with the predictions of the published criteria, such as the modified Mohr−Coulomb (MMC), Lou−Yoon−Huh, Hu, and Mu criteria.

2 Experimental

The studied in situ TiB_2/7075Al composite was synthesized by casting with a mixed salt route, and the composition is shown in Table 1. More details of the material preparation process can be found in the work of CHEN et al [23]. In order to

Table 1 Chemical composition of in situ TiB_2/7075Al composite (wt.%)

TiB_2	Cu	Mg	Zn	Zr	Al
6	2.4	2.5	6.9	0.15	Bal.

investigate the mechanical responses and failure of the composite in different stress states, various mechanical tests, including uniaxial tensile tests, notch tensile tests, compressive tests, and shear tests, were carried out at room temperature. Figure 1 shows the geometries and dimensions of the specimens. Before the mechanical tests, all the specimens were finely polished to eliminate machining defects, and the graphite was used to lubricate the specimen/anvil interface for compressive tests.

The mechanical tests were performed on an electronic testing machine (Instron Model 8080 with a load cell of 100 kN capacity) at a constant cross-head speed of 1 mm/min. A DIC system (Aramis) was employed to measure the deformation and strain field of the tensile and shear tests; the experimental setup is shown in Fig. 1. Prior to the tests, the specimens were uniformly sprayed with random speckle patterns. The three-dimensional position change of the speckles was photographed by two high-resolution cameras at a frequency of 5 Hz. The strain field of the deformed specimens was computed by the commercial DIC software GOM. At least three specimens were tested for each stress state, and all the specimens were strained to fracture. After the tests, the macroscopic and microscopic fractographs were characterized by an optical microscope (Leica M125) and a field-emission SEM (VEGA 3), respectively.

3 Numerical simulations for estimating state variables of fracture

Although the strain distribution of the in situ TiB_2/7075Al composite in different stress states can be captured by DIC experiments, it is difficult to obtain the stress state in the stress concentration areas. In this work, finite element (FE) simulations via ABAQUS/Standard were jointly used to characterize the deformation and stress distribution of the specimens under each loading condition. The fracture position was obtained from the DIC experiment, and the maximum equivalent plastic strain in the fracture path was taken as the fracture initiation point in the simulation. The stress state related to ductile fracture was extracted from this point.

The composite is supposed to follow an isotropic linear elastic-plastic material law; its macroscopic plastic behavior was modeled with the classic J_2 constitutive model. The elastic modulus E_c and Poisson ratio μ_c of the composite were obtained by the Taylor homogenization method as follows [24]:

$$E_c=(1-\varphi)E_m+\varphi E_p \quad (1)$$

$$\mu_c=(1-\varphi)\mu_m+\varphi\mu_p \quad (2)$$

where E_m and E_p are the elastic moduli of the matrix and the particle, respectively, μ_m and μ_p are the

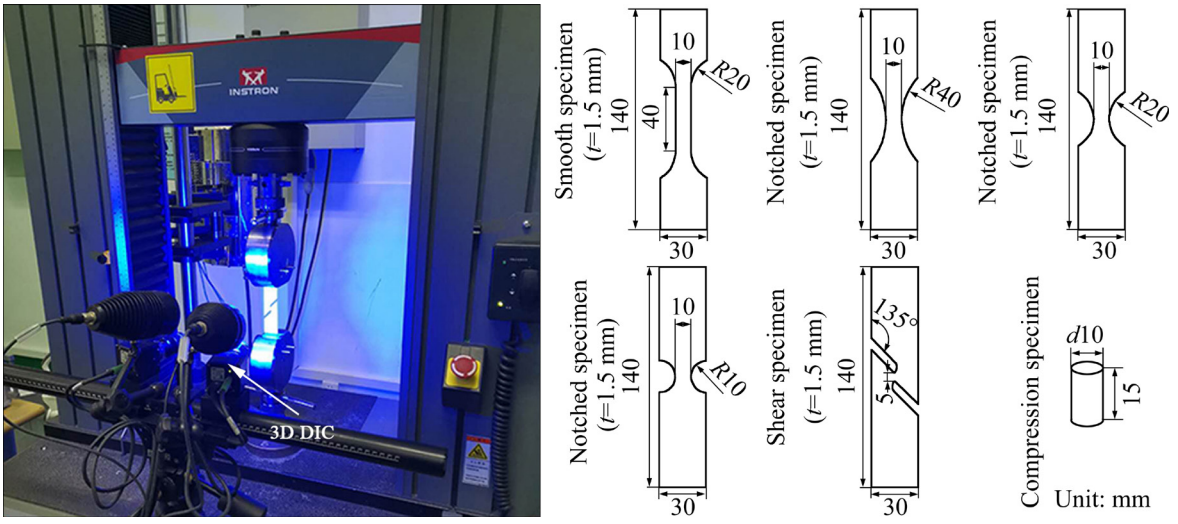

Fig. 1 Experiment setup with DIC system and geometrical dimensions of specimens for mechanical tests, including uniaxial tensile, notched tensile (with the notched radius of R=10, 20, and 40 mm, respectively), shear and compression tests (All these tests were carried out at room temperature to model the influence of stress states in a wide range, and t is the thickness of specimens)

corresponding Poisson ratios, and φ is the volume fraction of particles. For the composite studied, φ is about 4%, and the room temperature elastic constants of the 7075Al matrix are E_m=71 GPa and μ_m=0.33, and those of TiB_2 are E_p=560 GPa and μ_p=0.11 [25]. As a result, the elastic constants of the composite were calculated to be E_c=91 GPa and μ_c=0.32.

The work hardening law of the composite was derived from the uniaxial tensile results. To obtain the flow stress curve of the composite under large strain, a double Voce model (Eq. (3)) was used to fit the stress−strain data of the uniaxial tensile tests [26]. The double Voce model reads as

$$\sigma=\sigma_y+B_1[1-\exp(-k_1\varepsilon^p)]+B_2[1-\exp(-k_2\varepsilon^p)] \quad (3)$$

where σ is the stress, σ_y, B_1, B_2, k_1 and k_2 are material parameters, and ε^p is the equivalent plastic strain. The flow stress of the composite after necking was then extrapolated by the model, and the entire true stress−strain curve is shown in Fig. 2.

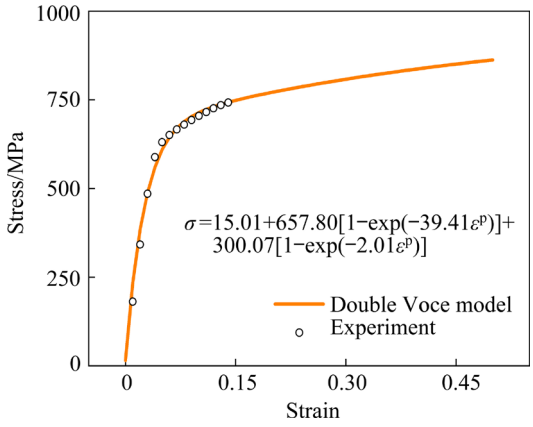

Fig. 2 Uniaxial true stress−strain curve of in situ TiB_2/7075Al composite under large deformation (The stress after necking was extrapolated by the double Voce model)

As shown in Fig. 3, FE geometrical models for a quarter of the smooth specimen and three notched specimens were established according to the symmetry in length and width directions. For the shear specimen and the compression specimen, complete models were established. In the compression test, the platen was treated as a rigid body, and the friction coefficient between the platen and the specimen was set to be 0.08. All the FE models were meshed with the general linear brick element with reduced integration (C3D8R), and the default hourglass control was employed. To achieve a compromise between computational efficiency and accuracy, fine meshing is used in the potential high stress regions. The boundary conditions employed in the simulation are also shown in Fig. 3. In the tensile tests of the smooth specimen, three notched specimens, and shear specimen, reference nodes were coupled with the loading surface. In the compression specimen, the reference node was coupled with the platen. In simulations, displacement boundary conditions were imposed.

4 Experimental and FEM results

4.1 Strain fields of specimens in different stress states

The DIC results of the strain fields for tests in different stress states are shown in Fig. 4. The smooth specimen exhibits a quite uniform strain distribution, and the strain localization appears with the startup of fracture. By contrast, all the notched specimens show significant strain localization during the loading process. The largest strain appears at the narrowest cross-section. For the shear specimen, deformation is fairly localized in the shear section.

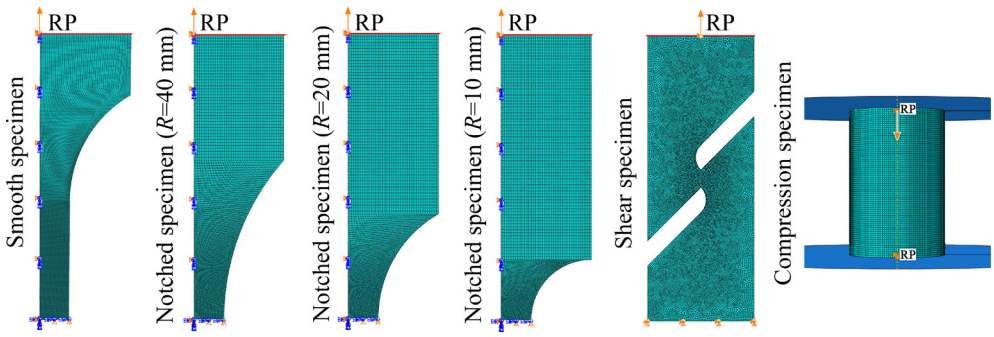

Fig. 3 FE models for tests in different stress states, including uniaxial tensile, notched tensile (with R=10, 20, and 40 mm, respectively), shear and compressive tests (For the smooth and three notched specimens, quarter models were established due to the symmetry. Complete models were used for the shear and compression specimens)

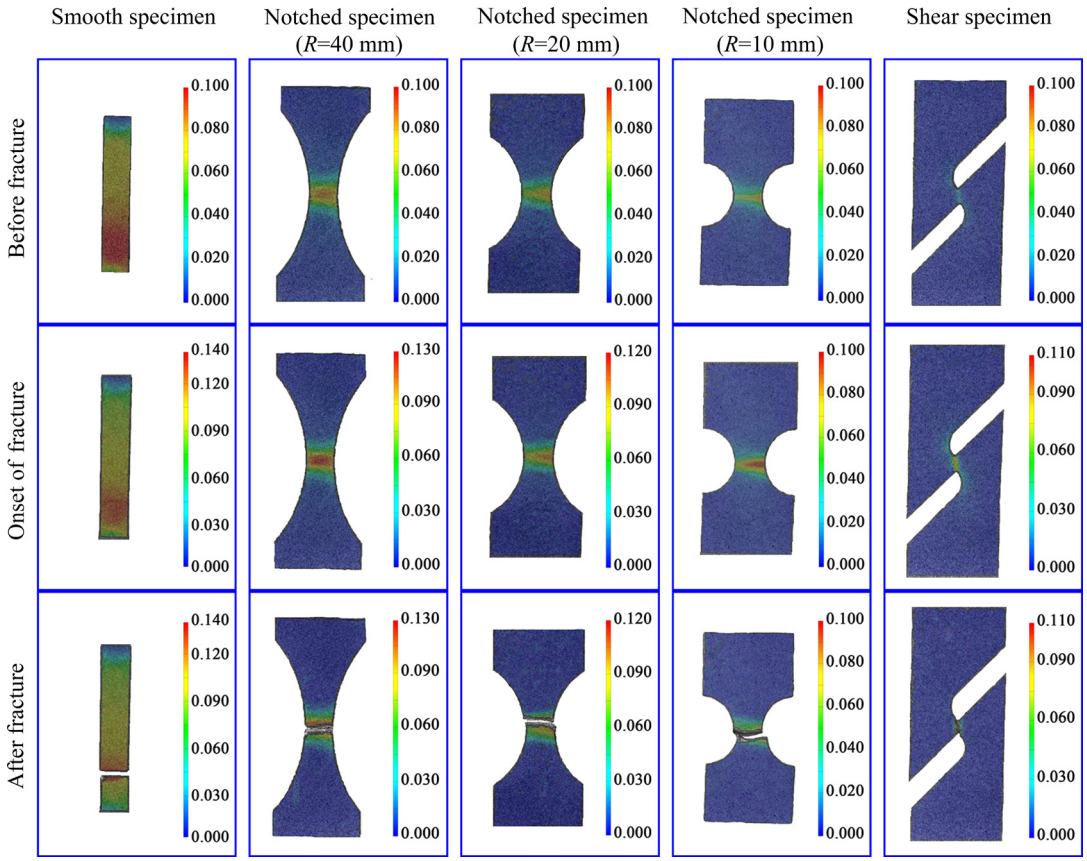

Fig. 4 DIC results for strain fields (von Mises equivalent strain) of five tests

4.2 Stress states and strain evolution before ductile fracture at fracture initiation point

As stated, FE simulations were carried out to predict the strain and stress distributions of all the experimental specimens. The simulation results are shown in Figs. 5 and 6. For each specimen, the load−displacement curves of the FE simulations agree well with the experimental ones. In addition, the strain distribution maps obtained by the DIC measurements are consistent with the simulation results. For the tensile tests, as shown in Figs. 5 and 6(a), the stress triaxiality increases with the decrease of the notched radius, while the Lode parameter almost has no change; for the shear test, as shown in Fig. 6(b), the stress state in the main deformation zone shows little change; for the compression test, as shown in Fig. 6(c), the stress triaxiality increases while the Lode parameter decreases with deformation.

During the simulation, when the imposed displacement reaches the experimental fracture displacement of the specimen, the fracture is considered to occur. Fracture strain is the equivalent plastic strain at the fracture initiation point in the simulation. The averaged stress triaxiality (η_{ave}) and the Lode parameter (ξ_{ave}) are selected as the representative parameters of stress state.

$$\eta_{\text{ave}} = \frac{1}{\bar{\varepsilon}^{\text{f}}} \int_0^{\bar{\varepsilon}^{\text{f}}} \eta \, \mathrm{d}\varepsilon \tag{4}$$

$$\xi_{\text{ave}} = \frac{1}{\bar{\varepsilon}^{\text{f}}} \int_0^{\bar{\varepsilon}^{\text{f}}} \xi \, \mathrm{d}\varepsilon \tag{5}$$

The determined η_{ave}, ξ_{ave} and the equivalent plastic strain to fracture $\bar{\varepsilon}_1^{\text{f}}$, $\bar{\varepsilon}_2^{\text{f}}$ and $\bar{\varepsilon}_3^{\text{f}}$ corresponding to the tensile, shear and compressive tests are listed in Table 2. As shown in Table 2, the influences of shear stress are similar in four groups of tensile specimens ($\tau_{\max}/\bar{\sigma}$ around 0.5). The fracture strain of the tensile specimens is mainly affected by the tensile stress, which decreases with the increase of $\sigma_1/\bar{\sigma}$. Compared with the tensile specimens, the shear specimen has a smaller $\sigma_1/\bar{\sigma}$, but an obviously larger $\tau_{\max}/\bar{\sigma}$. This indicates that the ductile fracture of the shear specimen is more obviously affected by shear stress. In summary, the ductile fracture of the composite is affected by both the tensile stress and shear stress.

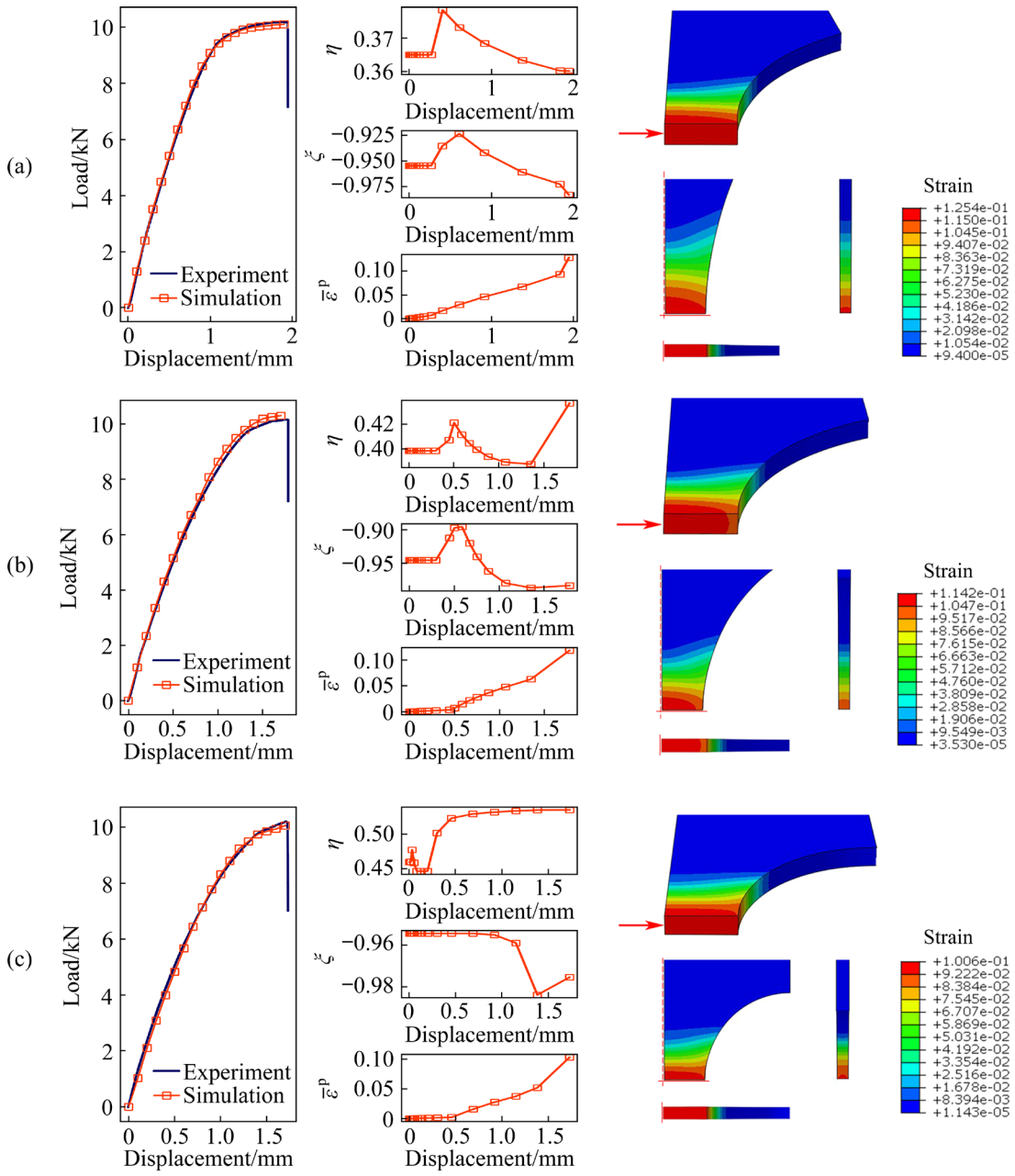

Fig. 5 FE simulation results for notched specimens with radii of 10 mm (a), 20 mm (b) and 40 mm (c) (The left plots show the comparison of load−displacement curves obtained from the experiments and FE simulations, and the evolution of stress triaxiality η, Lode parameter ξ, and equivalent plastic strain $\bar{\varepsilon}^{p}$ at the fracture initiation points with displacement. The right plots show the strain distribution maps predicted by the FE simulations, and the fracture initiation points are marked by the arrows)

4.3 Fracture mechanisms of composite

Figure 7 shows the macroscopic morphologies of the fracture specimens measured by an optical microscope (Leica M125). All the tensile specimens exhibit the failure mode of ductile fracture; the smooth specimen and notched specimens with different notch radii show similar macroscopic fractographs, which are slant and rough. The shear test specimen, nevertheless, exhibits quite different macroscopic fractograph; it is straight and smooth, manifesting the typical shear fracture characteristics. The change of fracture characteristics is related to the variation of stress state.

To explore the fracture mechanisms of the composite in different stress states, the microscopic fractographs of the tested specimens were further observed by SEM, as shown in Fig. 8. For each specimen, two images with a magnification of 2000

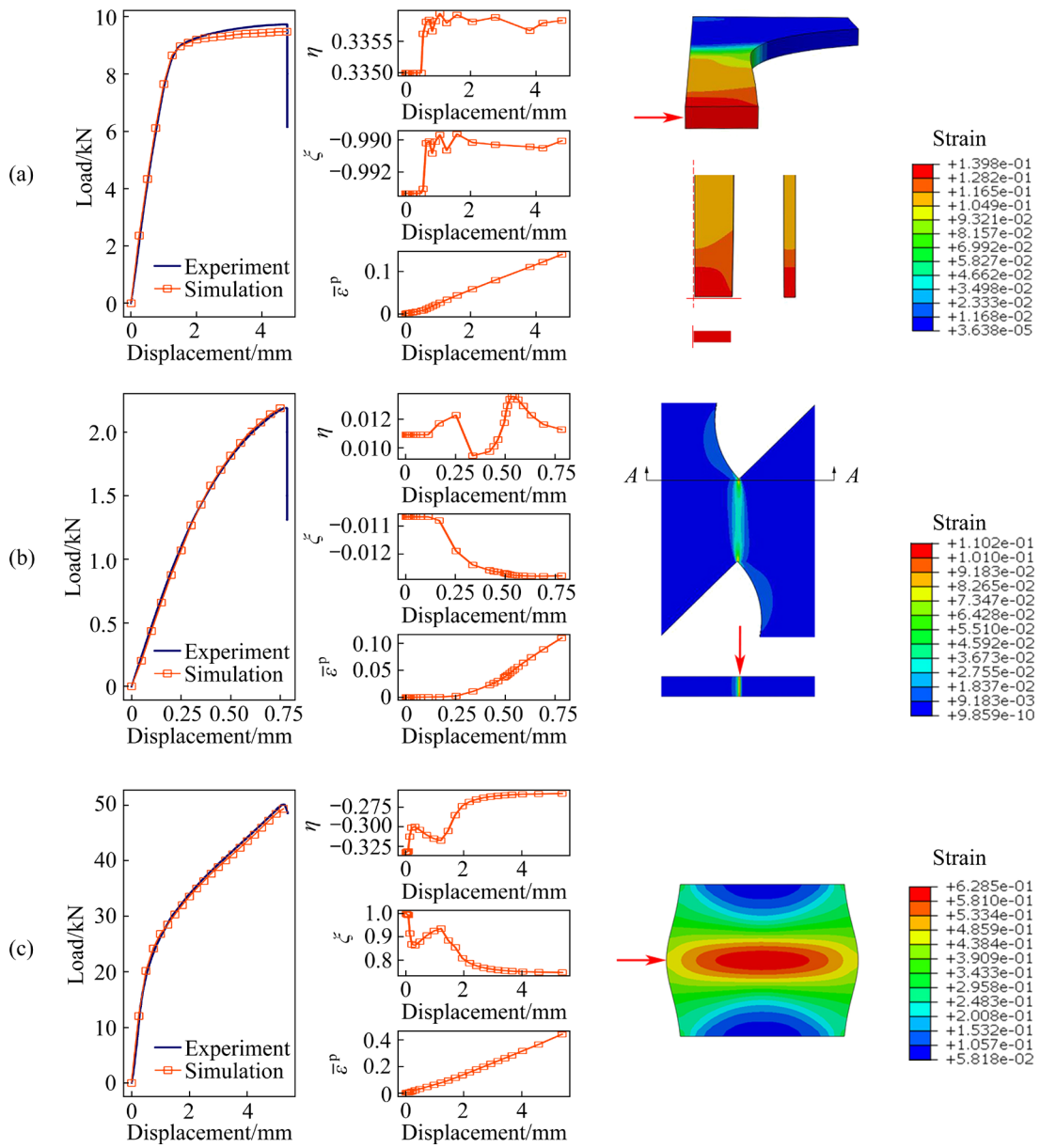

Fig. 6 FE simulation results for smooth specimen (a), shear specimen (b) and compression specimen (c) (The left plots show the comparison of load−displacement curves obtained from the experiments and FE simulations, and the evolution of stress triaxiality η, Lode parameter ξ, and equivalent plastic strain $\bar{\varepsilon}^p$ at the fracture initiation points with displacement. The right plots show the strain distribution maps predicted by the FE simulations, and the fracture initiation points are marked by the arrows)

Table 2 Stress triaxiality η_{ave}, Lode parameter ξ_{ave}, normalized maximum principal stress $\sigma_1/\bar{\sigma}$, normalized maximum shear stress $\tau_{max}/\bar{\sigma}$, and fracture strains $\bar{\varepsilon}_1^f$, $\bar{\varepsilon}_2^f$ and $\bar{\varepsilon}_3^f$ of specimens tested in different stress states

Specimen		η_{ave}	ξ_{ave}	$\sigma_1/\bar{\sigma}$	$\tau_{max}/\bar{\sigma}$	$\bar{\varepsilon}_1^f$	$\bar{\varepsilon}_2^f$	$\bar{\varepsilon}_3^f$
Smooth		0.336	−0.992	1.003	0.501	0.125	0.140	0.145
Notched	(R=40 mm)	0.366	−0.955	1.032	0.506	0.112	0.128	0.138
	(R=20 mm)	0.402	−0.950	1.068	0.506	0.109	0.119	0.132
	(R=10 mm)	0.501	−0.960	1.167	0.505	0.096	0.103	0.110
Shear		0.012	−0.012	0.591	0.577	0.096	0.110	0.116
Compression		−0.291	0.795	0.095	0.525	0.416	0.440	0.450

τ_{max} is the maximum shear stress, σ_1 is the maximum principal stress, and $\bar{\sigma}$ is the von Mises equivalent stress

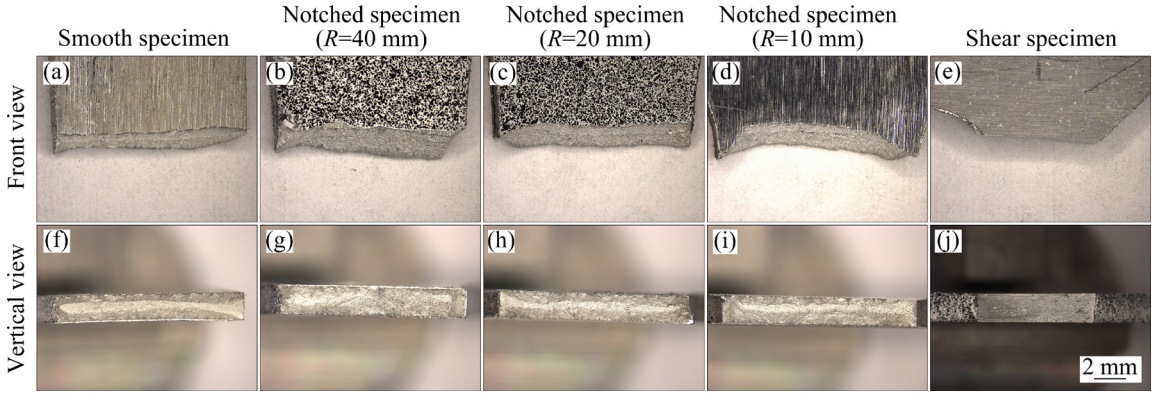

Fig. 7 Macroscopic fractographs of uniaxial tensile and shear specimens in different stress states

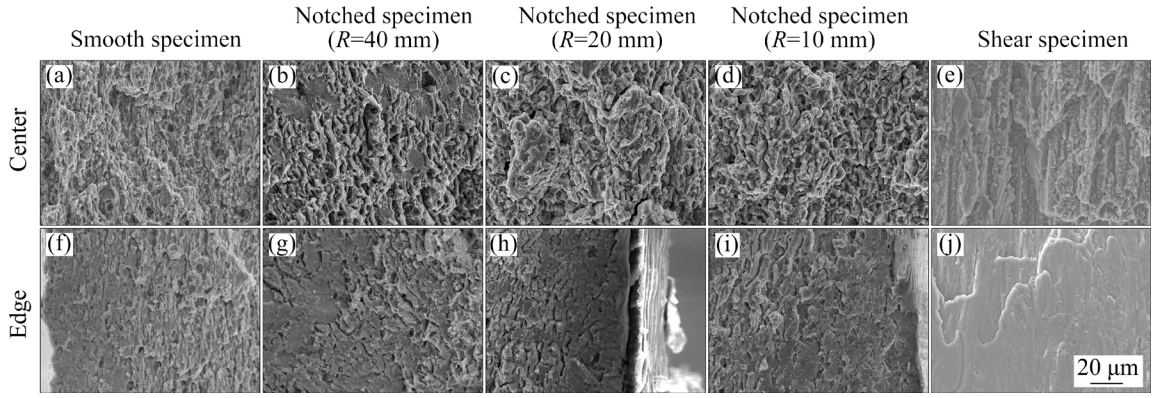

Fig. 8 SEM fractographs of tensile and shear specimens in different stress states

were photographed in the center and the edge regions. The microscopic fractographs of the tensile specimens are relatively rough, with many deep dimples in the central regions. By contrast, the microscopic fractograph of the shear specimen is smooth, with limited shallow and elongated dimples distributed in the shear direction. For the tensile specimens, with the decrease of the notch radius, the increased stress triaxiality facilitates the growth of voids. It thereby results in deep dimples and rough fractographs. More dimples exist in the central region than in the edges, demonstrating more pronounced nucleation and growth of voids in the center. For the shear specimen, due to the near-zero stress triaxiality, the nucleation and growth of voids are significantly suppressed; the fractographs thus show very shallow dimples or even no dimples.

The SEM backscattered electron (BSE) and the EDS images in the central regions of the tensile and the shear specimens are shown in Fig. 9. All the images were photographed with a magnification of 5000. The EDS characterization corresponds to the micro-chemical analysis of the element Ti, which is the dominant element of the particles. The fractographs of all five specimens exhibit obvious clustering of the element Ti (the yellow spots). It indicates the exposure of the TiB_2 particles and thereby the interface debonding during the fracture process. According to the BSE images, the broken particles appear in the fractographs of the tensile specimens; these phenomena indicate that particle fracture occurs in the condition of high stress triaxiality.

To further demonstrate the particle fracture in different stress states, the fractographs of the notched specimen (R=10 mm) and shear specimen were examined under high resolution, and the results are shown in Fig. 10. Obvious particle cracks are observed in the notched tensile test with high stress triaxiality and the shear test with low stress triaxiality.

Figure 11 shows the SEM fractographs of the compression specimen. As shown in Figs. 11(a) and (b), the compression specimens primarily exhibit similar fractographs as the shear specimen; the

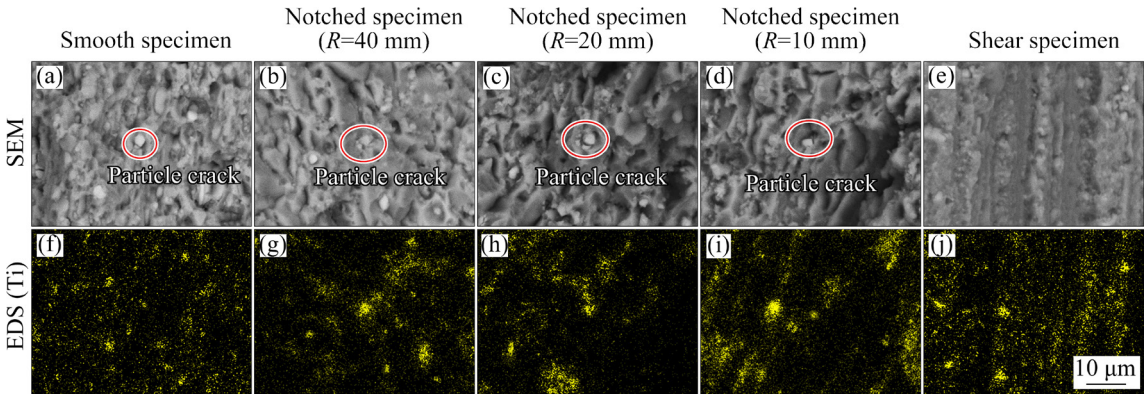

Fig. 9 SEM backscattered electron (BSE) and EDS images of tensile and shear specimens (The red circles highlight the particle crack on the fractographs; the yellow spots in the EDS images denote element Ti)

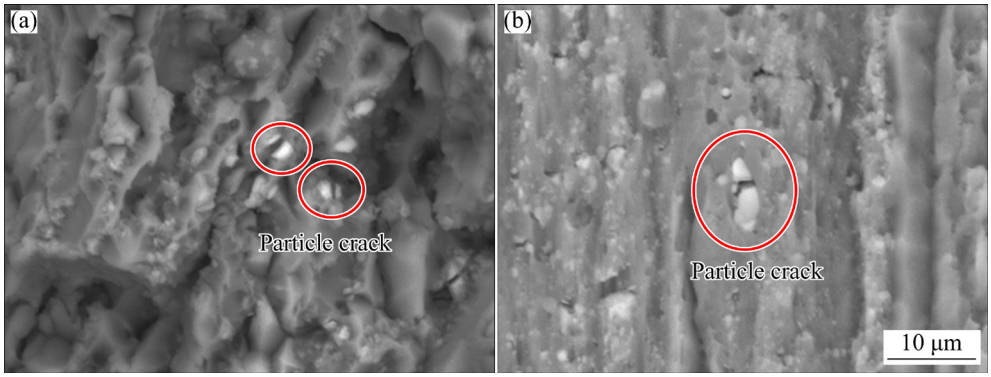

Fig. 10 SEM BSE images showing fractographs of notched specimen (R=10 mm) (a) and shear specimen (b) (The red circles highlight the particle crack on the fractographs)

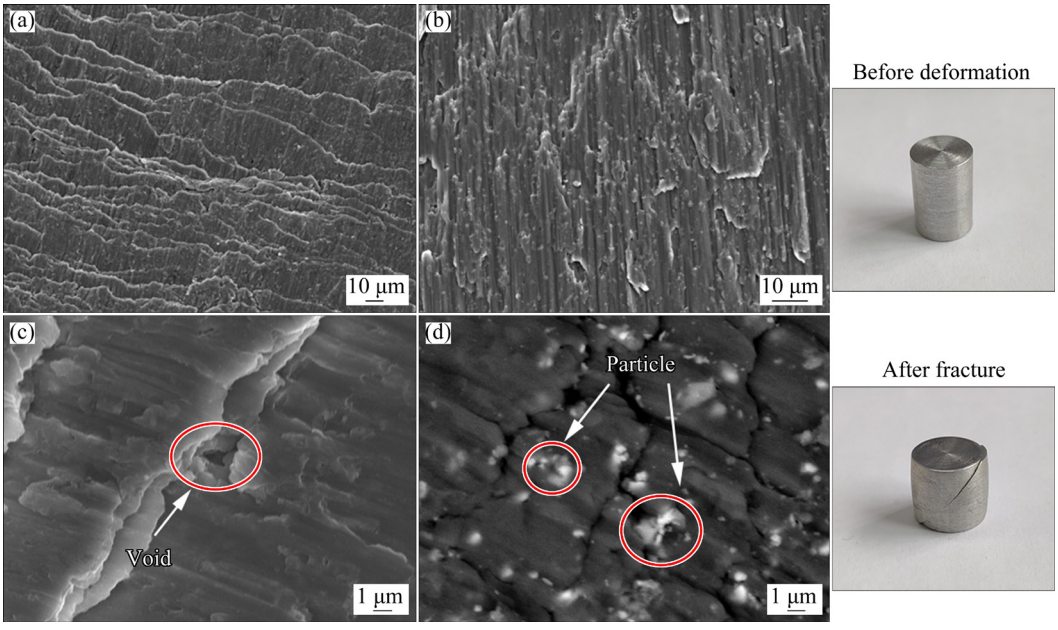

Fig. 11 SEM (a−c) and SEM SBE (d) images showing fractographs of compression specimen

surfaces are quite smooth and have limited shallow and elongated dimples distributed in the fracture direction. The magnified image shown in Fig. 11(c) evidences the formation of voids on the smooth fractograph. Consequently, the composite shows the same fracture mechanism in the shear and compression deformation modes. Specifically, its damage is manifested with shear fracture and limited dimples and voids. The BSE image, as shown in Fig. 11(d), demonstrates the exposure and

fracture of TiB_2 particles. Thus, both the interface debonding and particle fracture facilitate the formation of voids and promote the propagation of cracks.

Since the compression deformation results in a negative stress triaxiality, which will suppress the growth of voids, the voids are elongated in the shear direction, with a direction of 45° with respect to the compression direction. The results show that the composite has the same evolution mechanism of voids under the shear and compression deformation conditions.

The results of the fractographs for the six tests in different stress states are summarized in Table 3.

Table 3 Results of fractographs for six tests with different stress states

Experiment	Fractograph	Void evolution direction
Smooth specimen, tension	Deep dimples	Tensile direction
Notched specimen (R=40, 20, 10 mm), tension	Deep dimples	Tensile direction
Shear specimen	Shallow dimples	Shear direction
Compression specimen	Shallow dimples	Shear direction

In conclusion, all the tensile specimens show rough fractographs with many deep dimples. Both the shear and compression specimens show smooth fractographs, with limit shallow and elongated dimples distributed in the shear direction. Interface debonding and particle fracture exist in all the stress states, and they are the main void nucleation mechanisms of the composite. After the nucleation of voids, the composite shows two kinds of void evolution mechanisms with the increase of deformation: the tensile fracture mechanism under high stress triaxiality and the shear fracture mechanism under low stress triaxiality. The former is accompanied with an obvious volume expansion of voids, while the latter with the shape change of voids. These two evolution mechanisms were also reported by WECK and WILKINSON [27] and JIA and POVIRK [28] for traditional metal materials.

5 New ductile fracture criterion for PR-AlMCs

During the plastic deformation of metals and alloys, inhomogeneous deformation occurs between the matrix and the inclusions or the second-phase particles for their different mechanical properties; it facilitates the interface debonding that serves as the nucleation sites of voids. In addition, in the case of high strength matrix, the second-phase particles are prone to brittle fracture, also promoting the void nucleation in the matrix. As mentioned above, our experimental results verify that the main void nucleation mechanisms of the composite are interface debonding and particle fracture.

In general, tensile and shear stresses compete with each other to influence the ductile fracture of materials. ACHOURI et al [29] performed in situ experiments to observe these deformation patterns. In the tensile test, with the increase of plastic deformation, the initial spherical void gradually expanded into an ellipsoid along the direction of maximum principal stress. In contrast, in the shear test, the smooth fractograph kept parallel to the plane with maximum shear stress. Voids were elongated in the direction of maximum shear stress. As discussed above, the composite shows two mechanisms of ductile fracture. In the case of tensile fracture, the nucleated voids expand under the action of the maximum principal stress. In the case of shear fracture, the nucleated voids show significant shape change with the maximum shear stress, but no significant volume change.

5.1 New criterion for PR-AlMCs

As stated, the nucleation and evolution of voids of the composite are controlled by both the tensile stress and shear stress. Thus, a new phenomenological ductile fracture criterion can be proposed as

$$\left[\left(\frac{2\tau_{\max}}{\bar{\sigma}}\right)^{C_1}+\langle\frac{\sigma_1}{\bar{\sigma}}\rangle\right]^{C_2}\bar{\varepsilon}^{\mathrm{f}}=C_3 \tag{6}$$

where C_i (i=1, 2, 3) are material parameters and $\langle x\rangle$=1/2(x+|x|). Here, we supposed an equal influence of the tensile stress and shear stress on damage evolution.

In the case of non-proportional loading or non-linear plastic deformation, Eq. (6) is modified into an integral form as follows:

$$\int_0^{\bar{\varepsilon}^{\mathrm{f}}}\left[\left(\frac{2\tau_{\max}}{\bar{\sigma}}\right)^{C_1}+\langle\frac{\sigma_1}{\bar{\sigma}}\rangle\right]^{C_2}\mathrm{d}\bar{\varepsilon}^{\mathrm{p}}=C_3 \tag{7}$$

where σ_1 and τ_{max} can be represented by the stress triaxiality η, Lode parameter ξ, and equivalent stress $\bar{\sigma}$ as follows:

$$\sigma_1 = \left(\eta + \frac{3-\xi}{3\sqrt{\xi^2+3}}\right)\bar{\sigma} \tag{8}$$

$$\tau_{max} = \frac{1}{\sqrt{\xi^2+3}}\bar{\sigma} \tag{9}$$

Substituting the three principal stresses into Eq. (6) yields

$$\bar{\varepsilon}^f = \frac{C_3}{\left[\left(\frac{2}{\sqrt{\xi^2+3}}\right)^{C_1} + \langle\eta + \frac{3-\xi}{3\sqrt{\xi^2+3}}\rangle\right]^{C_2}} \tag{10}$$

5.2 Sensitive analysis of parameters

To classify the influences of the material parameters C_1−C_3 on the fracture initiation in the space (η, ξ, and $\bar{\varepsilon}^f$). The predicted 3D fracture surfaces with different values of C_i are shown in Fig. 12. C_1 is introduced to the term of normalized maximum shear stress to modulate the influence of tensile stress and shear stress on ductile fracture, and its effect on the fracture surface is illustrated in Fig. 12(a). A larger C_1 indicates an increased role of the maximum shear stress τ_{max} and a decreased fracture strain. The fracture surface at $\xi=\pm1$ decreases with increasing C_1, and the gap between the surfaces of fracture strain at different C_1 increases with the decrease of stress triaxiality η. However, the fracture strain at $\xi=\pm1$ is independent of C_1. C_2 modulates the effects of the tensile stress and shear stress on the fracture strain, and its effect on the fracture surface is illustrated in Fig. 12(b). The fracture surface essentially shrinks with increasing C_2 except in two regions with low stress triaxiality. In the condition of high stress triaxiality, void growth is promoted. Hence increasing C_2 accelerates the ductile fracture of the material. In the condition of low stress triaxiality, void growth by tensile stress is inhibited, and the effect of shear stress will decrease if the absolute value of the Lode parameter becomes larger, hence increasing C_2 inhibits void evolution in the two regions with low stress triaxiality and high absolute value of Lode parameter. C_3 modulates the magnitude of fracture strain, and its effect is illustrated in Fig. 12(c). The influence of C_3 is much more distinct than C_1 or C_2, which modulates the 3D fracture surface by a linear multiplication operation.

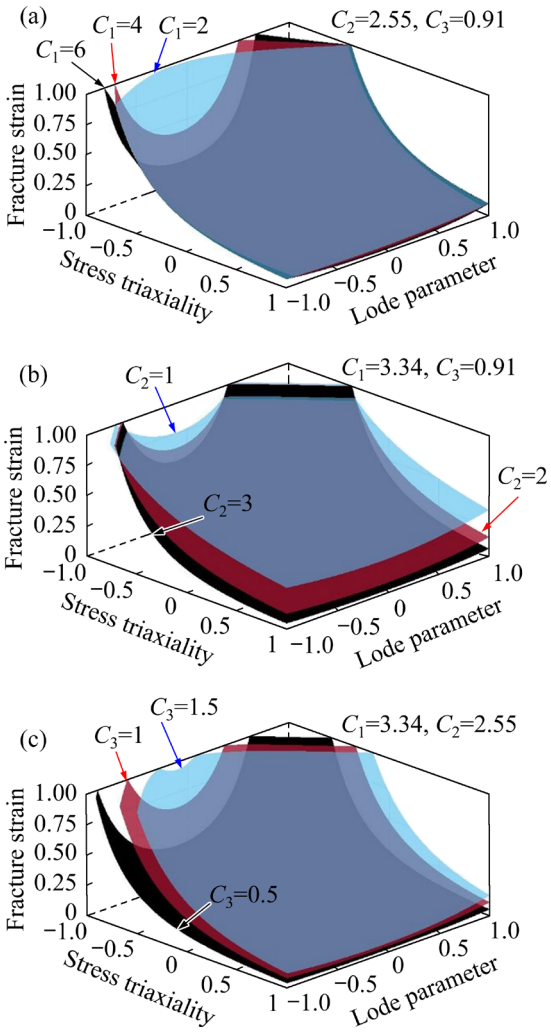

Fig. 12 Influences of parameters C_1 (a), C_2 (b), and C_3 (c) on predicted fracture surface of composite (Different colors represent fracture surfaces established with different values of the parameters)

6 Calibration and verification of proposed DFC

6.1 Calibration of DFC for in situ TiB_2/7075Al composite

Based on the data (η_{ave}, ξ_{ave}, and $\bar{\varepsilon}^f$) listed in Table 2 of the studied 18 tests, the parameters C_1, C_2, and C_3 were fitted using the least square method. The calibrated values are C_1=3.25, C_2=2.55 and C_3=0.80. The absolute relative error (δ_e) and average error (E_{err}) between the predicted and experimental fracture strains are defined as

$$\delta_e = \left| \frac{\bar{\varepsilon}^f_{pred}}{\bar{\varepsilon}^f_{exp}} - 1 \right| \times 100\% \quad (11)$$

$$E_{err} = \frac{\sum \delta_e}{N} \quad (12)$$

where N is the number of overall experiment.

The average error of the proposed DFC is 5.78%.

Figure 13 shows the 3D fracture surface predicted by the proposed DFC versus the experimental results. The predicted fracture surface well envelops all experimental points. Therefore, the criterion can predict the fracture strain of the composite in different stress states. For a constant Lode parameter, the proposed DFC predicts a monotonically decreasing fracture strain with increasing the stress triaxiality. As indicated by Eq. (8), the void evolution by tension mechanism, i.e., $\sigma_1/\bar{\sigma}$, demonstrates a positive correlation with η for a given ξ. Thus, a higher of η facilitates the growth of voids by tension mechanism, thereby reducing the ductility of the composite. Besides, for a constant stress triaxiality, the fracture strain decreases with the Lode parameter to zero. It is due to the increasing effect of the maximum shear stress.

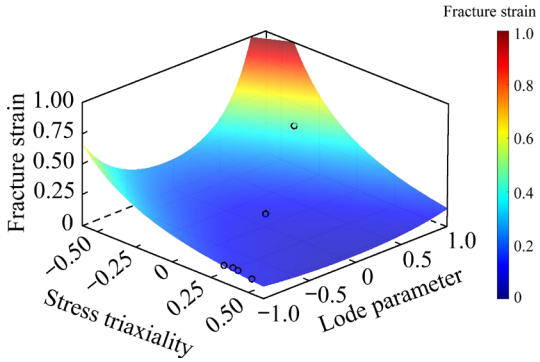

Fig. 13 3D fracture surface of in situ TiB_2/7075Al composite constructed by proposed criterion (The color spectrum indicates the fracture strain level from low (blue) to high (red); the black circles represent the experimental results in different stress states; the fracture surface well envelops all the experimental points)

6.2 Comparison with other criteria

The proposed criterion was further compared with DFCs reported in literature, i.e., the modified Mohr−Coulomb (MMC) [20], Lou−Yoon−Huh [22], Hu [30], and Mu [31] models. These models show good prospects for their simple structure and high prediction accuracy [32−34]. Details about these DFCs can be found in Appendix. Parameters of these criteria were calibrated by the same procedure described above; the average errors of the MMC, Lou−Yoon−Huh, Hu, and Mu criteria are 11.97%, 7.5%, 8.17%, and 6.54%, respectively. The 2D fracture curves predicted by these DFCs are shown in Fig. 14.

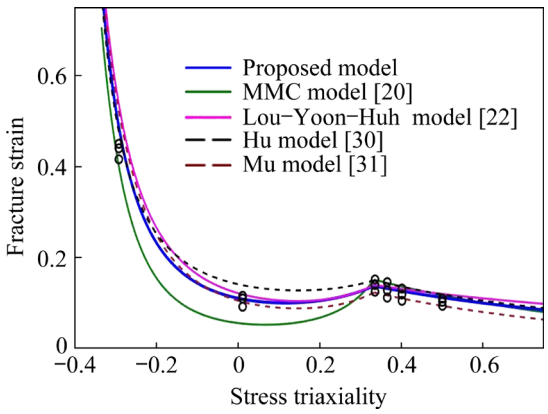

Fig. 14 2D fracture curves of in situ TiB_2/7075Al composite constructed by five DFCs (The black circles represent experimental results in different stress states)

The MMC model is an extension of the Mohr–Coulomb model, which was originally developed for brittle materials; the Lou−Yoon−Huh and Mu criteria, as well as the proposed criterion, are formulated in terms of the normalized maximum principal stress $\sigma_1/\bar{\sigma}$ and the maximum shear stress $\tau_{max}/\bar{\sigma}$; the Hu criterion uses the term $(\eta-1/3)$ to describe the influence of tensile stress on the growth of voids. As confirmed by our experiments, for all the studied stress states, the composite exhibits both the particle−matrix interface debonding and particle fracture, which are very different from those of single-phase materials. Since the proposed criterion considers the influence of both τ_{max} and σ_1, it agrees better with the experimental results. In addition, it was reported that the ductile fracture behavior of metals under tension-dominated states is different from that under compression-dominated states [35−37]; therefore, the proposed criterion, as an asymmetric one, could have a better application prospect. In the end, the MMC model assumes a power-type hardening behavior for materials. It is challenging to apply the MMC to the materials beyond the power hardening law characterization [38−40]. Other four DFCs, including the proposed one, by

contrast, are based on the micro-mechanisms of damage evolution without considering the strain hardening behavior of materials, thus have greater flexibility in applications [41].

7 Conclusions

(1) Under all the studied loading conditions, including smooth tension, notched tension, shear, and compression, the in situ TiB_2/7075Al composite shows two main fracture mechanisms of interface debonding and particle fracture, which facilitate the formation of voids and the propagation of cracks.

(2) The interface debonding and particle fracture of the composite are affected by both tensile stress and shear stress. For the tensile deformation, the nucleated voids expand obviously under the action of the maximum principal stress, which leads to rough fractographs filled with deep dimples. For the shear deformation, the nucleated voids exhibit significant shape change but little volume change under the action of the maximum shear stress, which leads to smooth fractographs with limited shallow and elongated dimples distributed in the shear direction.

(3) Based on the fracture mechanisms uncovered by the experiments, a modified ductile fracture criterion considering the influence of both maximum principal stress and maximum shear stress is developed specifically for the composite. The proposed DFC successfully predicts the fracture behavior of the composite in a wide range of stress states.

Acknowledgments

The authors gratefully acknowledge the financial support from the National Natural Science Foundation of China (No. 52075328), and Shanghai Rising-Star Program, China (No. 20QA1405300).

Appendix

Modified Mohr−Coulomb criterion (MMC) [20]:

$$\overline{\varepsilon}^{\mathrm{f}}=\left\{\frac{A}{C_2}\left[C_3+(2+\sqrt{3})(1-C_3)(\sqrt{\xi^2+3}-\sqrt{3})\right]\cdot\left[\sqrt{\frac{1+C_1^2}{\xi^2+3}}+C_1\left(\eta-\frac{\xi}{3\sqrt{\xi^2+3}}\right)\right]\right\}^{-1/n} \tag{A1}$$

Lou−Yoon−Huh criterion [22]:

$$\overline{\varepsilon}^{\mathrm{f}}=\frac{C_3}{\left\{\left(\frac{2}{\sqrt{\xi^2+3}}\right)^{C_1}\times\left[\frac{1}{1+C}\left(\eta+\frac{3-\xi}{3\sqrt{\xi^2+3}}+C\right)\right]^{C_2}\right\}} \tag{A2}$$

Hu criterion [30]:

$$\overline{\varepsilon}^{\mathrm{f}}=\frac{C_3}{\left[\left(\frac{2}{\sqrt{\xi^2+3}}\right)^{C_1}+\left(\eta-\frac{1}{3}\right)\right]^{C_2}} \tag{A3}$$

Mu criterion [31]:

$$\overline{\varepsilon}^{\mathrm{f}}=C_3\left[\frac{3\sqrt{\xi^2+3}}{C_1\left(3\eta\sqrt{\xi^2+3}-\xi\right)+3}\right]^{C_2} \tag{A4}$$

References

[1] IBRAHIM I A, MOHAMED F A, LAVERNIA E J. Particulate reinforced metal matrix composites—A review [J]. Journal of Materials Science, 1991, 26: 1137−1156.

[2] PRASAD S V, ASTHANA R. Aluminum metal–matrix composites for automotive applications: Tribological considerations [J]. Tribology Letters, 2004, 17: 445−453.

[3] LÜ L, LAI M O, SU Y, TEO H L, FENG C F. In situ TiB_2 reinforced Al alloy composites [J]. Scripta Materialia, 2001, 45: 1017−1023.

[4] MANDAL A, MAITI R, CHAKRABORTY M, MURTY B S. Effect of TiB_2 particles on aging response of Al−4Cu alloy [J]. Materials Science and Engineering: A, 2004, 386: 296−300.

[5] PANDEY A B, MAJUMDAR B S, MIRACLE D B. Deformation and fracture of a particle-reinforced aluminum alloy composite: Part I. Experiments [J]. Metallurgical and Materials Transactions A, 2000, 31: 921−936.

[6] LLOYD D J. Aspects of fracture in particulate reinforced metal matrix composites [J]. Acta Metallurgica et Materialia, 1991, 39: 59−71.

[7] DOEL T J A, BOWEN P. Tensile properties of particulate-reinforced metal matrix composites [J]. Composites Part A: Applied Science and Manufacturing, 1996, 27: 655−665.

[8] MAWSOUF N M. A micromechanical mechanism of fracture initiation in discontinuously reinforced metal–matrix composite [J]. Materials Characterization, 2000, 44: 321−327.

[9] KARBALAEI AKBARI M, BAHARVANDI H R, SHIRVANIMOGHADDAM K. Tensile and fracture behavior of nano/micro TiB_2 particle reinforced casting A356 aluminum alloy composites [J]. Materials & Design, 2015, 66: 150−161.

[10] WU S B, ARSENAULT R J. The fracture mode in SiC−Al

composites [J]. Materials Science and Engineering: A, 1991, 138: 227−235.

[11] GURSON A L. Continuum theory of ductile rupture by void nucleation and growth: Part I—Yield criteria and flow rules for porous ductile media [J]. Journal of Engineering Materials and Technology, 1977, 99: 2−15.

[12] LEMAITRE J. A continuous damage mechanics model for ductile fracture [J]. Journal of Engineering Materials and Technology, 1985, 107: 83−89.

[13] ZHANG Xue-min, ZENG Wei-dong, SHU Ying, ZHOU Yi-gang, ZHAO Yong-qing, WU Huan, YU Han-qing. Fracture criterion for predicting surface cracking of Ti40 alloy in hot forming processes [J]. Transactions of Nonferrous Metals Society of China, 2009, 19: 267−271.

[14] HU Xing, ZHAO Yi-xi, LI Shu-hui, LIN Zhong-qin. Numerical simulation of ductile fracture behavior for aluminum alloy sheet under cyclic plastic deformation [J]. Transactions of Nonferrous Metals Society of China, 2011, 21: 1595−1601.

[15] YU Hai-yan, WANG You. Bulging simulation of ductile fracture of 5052 aluminum alloy [J]. The Chinese Journal of Nonferrous Metals, 2015, 25: 2975−2981. (in Chinese)

[16] BAO Ying-bin, WIERZBICKI T. On fracture locus in the equivalent strain and stress triaxiality space [J]. International Journal of Mechanical Sciences, 2004, 46: 81−98.

[17] OYANE M, SATO T, OKIMOTO K, SHIMA S. Criteria for ductile fracture and their applications [J]. Journal of Mechanical Working Technology, 1980, 4: 65−81.

[18] XUE Liang. Damage accumulation and fracture initiation in uncracked ductile solids subject to triaxial loading [J]. International Journal of Solids and Structures, 2007, 44: 5163−5181.

[19] XUE Liang, WIERZBICKI T. Ductile fracture initiation and propagation modeling using damage plasticity theory [J]. Engineering Fracture Mechanics, 2008, 75: 3276−3293.

[20] BAI Yuan-li, WIERZBICKI T. Application of extended Mohr–Coulomb criterion to ductile fracture [J]. International Journal of Fracture, 2010, 161: 1−20.

[21] LOU Yan-shan, HUH H, LIM S, PACK K. New ductile fracture criterion for prediction of fracture forming limit diagrams of sheet metals [J]. International Journal of Solids and Structures, 2012, 49: 3605−3615.

[22] LOU Yan-shan, YOON J W, HUH H. Modeling of shear ductile fracture considering a changeable cut-off value for stress triaxiality [J]. International Journal of Plasticity, 2014, 54: 56−80.

[23] CHEN Z, SUN G A, WU Y, MATHON M H, BORBELY A, CHEN D, JI G, WANG M L, ZHONG S Y, WANG H W. Multi-scale study of microstructure evolution in hot extruded nano-sized TiB_2 particle reinforced aluminum composites [J]. Materials & Design, 2017, 116: 577−590.

[24] FLYNN J, AMIRI A, ULVEN C. Hybridized carbon and flax fiber composites for tailored performance [J]. Materials & Design, 2016, 102: 21−29.

[25] MUNRO R G. Material properties of titanium diboride [J]. Journal of Research of the National Institute of Standards and Technology, 2000, 105: 709−20.

[26] KOC P, ŠTOK B. Computer-aided identification of the yield curve of a sheet metal after onset of necking [J]. Computational Materials Science, 2004, 31: 155−168.

[27] WECK A, WILKINSON D S. Experimental investigation of void coalescence in metallic sheets containing laser drilled holes [J]. Acta Materialia, 2008, 56: 1774−1784.

[28] JIA S, POVIRK G L. Modeling the effects of hole distribution in perforated aluminum sheets. II: Minimum strength failure paths [J]. International Journal of Solids and Structures, 2002, 39: 2533−2545.

[29] ACHOURI M, GERMAIN G, DAL SANTO P, SAIDANE D. Experimental characterization and numerical modeling of micromechanical damage under different stress states [J]. Materials & Design, 2013, 50: 207−222.

[30] HU Qi, LI Xi-feng, HAN Xian-hong, CHEN Jun. A new shear and tension based ductile fracture criterion: Modeling and validation [J]. European Journal of Mechanics, 2017, 66: 370−386.

[31] MU Lei, ZANG Yong, WANG Yuan, LI Xiao-long, ARAUJO STEMLER P M. Phenomenological uncoupled ductile fracture model considering different void deformation modes for sheet metal forming [J]. International Journal of Mechanical Sciences, 2018, 141: 408−423.

[32] LIU Yan, KANG Lan, GE Han-bin. Experimental and numerical study on ductile fracture of structural steels under different stress states [J]. Journal of Constructional Steel Research, 2019, 158: 381−404.

[33] GHAZALI S, ALGARNI M, BAI Yuan-li, CHOI Y. A study on the plasticity and fracture of the AISI 4340 steel alloy under different loading conditions and considering heat-treatment effects [J]. International Journal of Fracture, 2020, 225: 69−87.

[34] DONG Guo-jiang, CHEN Zhi-wei, YANG Zhuo-yun, FAN Bo-cheng. Comparative study on forming limit prediction of AA7075-T6 sheet with M−K model and Lou−Huh criterion [J]. Transactions of Nonferrous Metals Society of China, 2020, 30: 1463−1477.

[35] ZHU Ya-zhi, ENGELHARDT M D. Prediction of ductile fracture for metal alloys using a shear modified void growth model [J]. Engineering Fracture Mechanics, 2018, 190: 491−513.

[36] LI Wen-chao, LIAO Fang-fang, ZHOU Tian-hua, ASKES H. Ductile fracture of Q460 steel: Effects of stress triaxiality and Lode angle [J]. Journal of Constructional Steel Research, 2016, 123: 1−17.

[37] LUO Tuo, GAO Xiao-sheng. On the prediction of ductile fracture by void coalescence and strain localization [J]. Journal of the Mechanics and Physics of Solids, 2018, 113: 82−104.

[38] QIAN Ling-yun, PAREDES M, WIERZBICKI T, SPARRER Y, FEUERSTEIN M, ZENG Pan, FANG Gang. Experimental and numerical study on shear-punch test of 6060 T6 extruded aluminum profile [J]. International Journal of Mechanical Sciences, 2016, 118: 205−218.

[39] QIAN Ling-yun, FANG Gang, ZENG Pan. Modeling of the ductile fracture during the sheet forming of aluminum alloy considering non-associated constitutive characteristic [J]. International Journal of Mechanical Sciences, 2017, 126: 55−66.

[40] JIA Yue-qian, BAI Yuan-li. Ductile fracture prediction for metal sheets using all-strain-based anisotropic eMMC model

[J]. International Journal of Mechanical Sciences, 2016, 115/116: 516−531.
[41] PARK N, HUH H, LIM S J, LOU Y S, KANG Y S, SEO M H. Fracture-based forming limit criteria for anisotropic materials in sheet metal forming [J]. International Journal of Plasticity, 2017, 96: 1−35.

原位 TiB_2 颗粒增强 7075 铝基复合材料在不同应力状态下的韧性断裂行为

王 涵，章海明，崔振山，陈 哲，陈 东

上海交通大学 材料科学与工程学院，上海 200240

摘 要：采用力学试验、微观表征和数值模拟研究原位 TiB_2 颗粒增强 7075 铝基复合材料在不同应力状态下的断裂行为。设计 4 组拉伸试样、1 组剪切试样和 1 组压缩试样，并对这 6 组试样进行力学实验。通过原位应变测试和有限元模拟研究 6 组试样在变形过程中的应变分布。对 6 组试样的断口形貌进行表征，分析其在不同应力状态下的损伤演化机制。研究发现：该材料的主要断裂机制为界面脱粘和颗粒断裂，表现为高应力三轴度下的拉伸断裂和低应力三轴度下的剪切断裂。在拉伸断裂条件下，形核空洞的体积在最大主应力的作用下增大；在剪切断裂条件下，空洞的形状在最大剪应力作用下变化明显，而体积变化不明显。基于实验揭示的断裂机理，提出一种考虑最大主应力和最大剪应力的韧性断裂准则，该准则可以预测该复合材料在不同应力状态下的断裂曲面。与改进的 Mohr−Coulomb、Lou−Yoon−Huh、Hu 和 Mu 模型的对比分析表明，新模型能更准确地预测铝基复合材料的韧性断裂行为。

关键词：铝基复合材料；韧性断裂准则；界面脱粘；颗粒断裂

(Edited by Wei-ping CHEN)